Ocean Engineering 363 (2026) 126582

Contents lists available at ScienceDirect

Ocean Engineering

journal homepage: www.elsevier.com/locate/oceaneng

Research paper

Influence of rotor skew angles on underwater noise source characteristics of pump-jet propulsor

Chao Chen [a], Jie Zhu [b], Liushuai Cao [a,*], Decheng Wan [a]

[a] Computational Marine Hydrodynamic Lab (CMHL), School of Ocean and Civil Engineering, Shanghai Jiao Tong University, Shanghai, 200240, China
[b] Wuhan Second Ship Design and Research Institute, Wuhan, 430064, China

ARTICLE INFO

Keywords:
Underwater noise
Sound source
FW-H acoustic analogy
Pump-jet propulsor
Skew angles

ABSTRACT

This study first employs the Improved Delayed Detached Eddy Simulation (IDDES) method to analyze the flow of a pump-jet propulsor (PJP) at three different rotor skew angles: 0°, 30°, and 60°. Subsequently, based on the Ffowcs Williams–Hawkings (FW-H) acoustic analogy method, the flow noise is computed, and both the far field acoustic characteristics and near field noise source distribution are investigated. The results show that as the skew angles increase, the efficiency of the PJP also increases, with a maximum improvement of 5.57%. For the far field noise monitoring points located laterally and rearward, the overall sound pressure level (OASPL) generated by the quadrupole source decreases with increasing skew angles. In the low-frequency range of 0~300 Hz, the sound pressure level (SPL) for all three skew angles exhibits similar attenuation rates. Using the dipole and quadrupole sound source extraction method presented in this study, distinct dipole and quadrupole characteristics can be observed on the tip vortices in the wake field, and quadrupole features are also prominent at the leading edges of both the rotor and stator blades. The findings of this study could provide some insights into the noise mechanism of PJP and offer a reference for noise control technologies.

1. Introduction

In the field of marine engineering research, the pump-jet propulsor (PJP) is a highly efficient propulsion technology widely used in applications that require low noise levels, such as military submarines and unmanned underwater vehicles (Shi et al., 2022). Compared to conventional propellers, the PJP not only provides higher thrust but also offers better noise control advantages (Cokmick and Eisenhuth, 1963). However, despite its advantages, the PJP still generates underwater noise in practical applications, which can have potential impacts on stealth performance and the marine ecosystem. Therefore, studying the underwater flow noise characteristics and mechanisms of the PJP is of significant importance for enhancing its acoustic performance and expanding noise control methods (Wu et al., 2023; Zhang et al., 2023).

Some studies have already been conducted on the underwater flow noise characteristics of the PJP. Zheng et al. (2024) equipped the hub of the PJP with two types of propeller boss cap fins (PBCF) and performed numerical calculations of the flow noise for these two configurations based on the Ffowcs Williams–Hawkings (FW-H) acoustic analogy method. The results showed that the fixed PBCF modifies the characteristics of the line spectrum noise but leads to an increase in flow noise. In contrast, the rotating PBCF increases the rotor's thrust coefficient by 2.03% to 3.15%, while reducing both the exciting force and the line spectrum noise. Li et al. (2025) combined the IDDES method with the acoustic analogy approach to investigate the effect of duct parameters on the flow noise of the PJP under both self-propulsion and open-water conditions. They found that the change trends of the PJP vortex system and flow noise under different duct parameters are not entirely consistent. Strong vortices within the PJP wake are positively correlated with higher flow noise when there is no separated flow over the duct. Yang et al. (2024) designed two types of serrated structures at the trailing edge of the duct of a pump-jet propulsor and investigated their noise reduction effects. They found that the vortex-disruption capability of the serrated trailing edge contributes to a decrease in the noise level of the two PJP configurations with serrated trailing edges within the frequency range of 0~1000 Hz. The most substantial noise reduction, up to 4.43 dB, was observed at the rear of the PJP. Although the SPL showed a slight increase at certain locations, this increase remained below 0.5 dB, which is considered negligible in the overall context. Qin et al. (2019) also investigated the noise reduction effects of

This article is part of a special issue entitled: OE_Marine Hydrodynamic Noise published in Ocean Engineering.
* Corresponding author.
E-mail address: liushuaicao@sjtu.edu.cn (L. Cao).

https://doi.org/10.1016/j.oceaneng.2026.126582
Received 29 March 2026; Received in revised form 11 June 2026; Accepted 14 June 2026
Available online 19 June 2026
0029-8018/

a sawtooth structure at the trailing edge of the duct and found that the sawtooth duct can significantly reduce the noise generated by the PJP from 10 Hz to 5000 Hz, particularly in the low-frequency range below 1000 Hz. The OASPL of the PJP is reduced by approximately 2.5~5 dB with the maximum reduction of 4.88 dB observed at the design point.

The aforementioned studies on the flow noise of the PJP indicate that the FW-H acoustic analogy method has been widely applied. On the other hand, these studies also highlight that, due to the more complex structure of the PJP, its generated flow noise is influenced by more factors compared to traditional propellers, such as duct shape, advance ratio, blade shape and so on.

The rotor, stator, and duct are fundamental components of the PJP. The skew angle of the rotor, as one of the most basic and important parameters in propulsor design, plays a crucial role in influencing both the hydrodynamic and acoustic performance of the propulsor. Yu et al. (2023) investigated the loading noise generated by two types of propellers, one with no skew and one with skew, under non-uniform inflow conditions. They found that, compared to the non-skewed propeller, the noise level of the skewed propeller decreases by 9~10 dB near the axial direction but increases at specific radiation directions. Furthermore, it was observed that the effect of the skew on the tonal noise decreased as the advance speed increased. Hadipour et al. (2021) investigated the underwater noise of a 7-blade high skew marine propeller under three different advance ratios. They found that the oscillation of the noise generated at the leading edge of the propeller is greatest, with the highest intensity occurring at an advance ratio of $J = 0.34$. The lowest amount of noise energy was produced at the trailing edge. Additionally, maximum noise levels were observed at frequencies of 4, 100, and 120 Hz at the tip, and at frequencies of 4 and 18 Hz at the leading edge. Tong et al. (2021) investigated the relationship between the modal characteristics of a 6-blade high skew marine propeller and the radiated noise. They found that the dominant and coupled modes of the propeller are excited by the broadband thrust, but only the dominant modes contribute to the radiated noise. As the advance ratio increases from 13.33 to 20, the radiated noise power from the propeller's vibration more than doubles. Additionally, the influence of the integral length on the radiated noise power depends on the blade spacing.

Current research on the impact of rotor skew angles on noise primarily focuses on traditional propellers, with fewer studies conducted on PJP. Additionally, most of the existing research concentrates on the acoustic characteristics at far-field monitoring points. In fact, the structure of the PJP first affects the near-field noise sources, which then radiate to the far-field monitoring points. Investigating the mechanisms of near-field noise sources can enrich the noise design theory for PJP and provide valuable insights for the development of noise control technologies. Yu et al. (2025a,b) studied the sound source distribution of the NACA 0012 airfoil at different Reynolds numbers and found that, with the attack angle, the quadrupole begins to shift towards the suction side at approximately 5°. The pressure fluctuation dominant mode is similar to that of the Lighthill source. The peak frequency of the quadrupole corresponds to the frequency of the high-energy vorticity mode. Additionally, the quadrupole is distributed widely downstream, similar to the acoustic directivity. Turner et al. (2022) performed direct numerical simulations of low-speed flow around the NACA 0012 airfoil at attack angles of 0°, 5°, and 10°, revealing significant differences in the quadrupole contributions, including changes in the major source locations and frequencies. They found that the inclusion of quadrupole sources results in an increase in the predicted noise power level across all frequencies, varying between 2 and 8 dB, compared to the dipole-only case. The quadrupole contribution is far from negligible, even at low subsonic speeds (Mach 0.3 and 0.4) when airfoil stall occurs. Yu et al. (2025a,b) investigated the sphere, dipole, and quadrupole sound sources generated by cavitating propellers and found that the lower the cavitation number, the higher the surface force fluctuations, which is reflected in the increased dipole intensity. The vortex affects the turbulence in the wake region, contributing to the quadrupole source. The cavitation behavior influences the sphere pressure, with a stronger sphere source observed when the cavitation number is smaller and the standard deviation of the cavitation area is larger.

Previous studies on sound sources primarily focus on airfoils and traditional propellers, with limited studies on the flow and noise mechanisms of PJP, particularly regarding the effects of variations in a single geometric parameter on acoustic characteristics. Therefore, this study, based on the IDDES method and the FW-H acoustic analogy, investigates the impact of rotor skew angles on both the far-field acoustic characteristics and near-field sound source distribution of the PJP. The findings could provide insights for the analysis of PJP noise mechanisms and the development of noise control technologies. The structure of this study is as follows: Section 2 introduces the numerical theory, including the turbulence model, the FW-H equation, and near-field sound sources. Section 3 presents a numerical verification of the hydrodynamic performance, including grid uncertainty analysis and validation of the open-water curve. Section 4 presents the numerical results and discussion, including an analysis of the flow field, far-field acoustic characteristics, and near-field sound sources. Section 5 concludes the study.

2. Numerical methodology

2.1. Governing equations

In this study, the fluid is single-phase, incompressible water. The tensor form of the RANS equations is expressed as follows:

$$\frac{\partial u_i}{\partial x_i} = 0 \tag{1}$$

$$\frac{\partial(\rho u_i)}{\partial t} + \frac{\partial}{\partial x_j}(\rho u_i u_j) = -\frac{\partial p}{\partial x_i} + \frac{\partial}{\partial x_i}\left[\mu\left(\frac{\partial u_i}{\partial x_j} + \frac{\partial u_j}{\partial x_i}\right) - \rho\overline{u_i' u_j'}\right] + S_j \tag{2}$$

where the x_i and x_j ($i, j = 1, 2, 3$) refer to the coordinate components. u_i and u_j refer to freestream velocity components. ρ is the fluid density, p is the pressure, and u_i'、 u_j' denote the fluctuating velocity components. S_j is a generalized source term.

To close the above equations, An Improved Delayed DES method (IDDES) based on $k-\omega$ shear stress transport (SST) turbulence model (Menter et al., 1994) was employed in this study. It is widely used in the field of rotating machinery, the equation form is as follows (Shur et al., 2008):

$$\frac{\partial \rho k}{\partial t} + \nabla\cdot(\rho\vec{u}k) = \nabla\cdot[(\mu+\sigma_k\mu_t)\nabla k] + P_k - \frac{\rho\sqrt{k^3}}{l_{IDDES}} \tag{3}$$

$$\frac{\partial \rho\omega}{\partial t} + \nabla\cdot\left(\rho\vec{u}\omega = \nabla\cdot[(\mu+\sigma_\omega\mu_t)\nabla\omega] + 2(1-F_l)\rho\sigma_{\omega 2}\frac{\nabla k - \nabla\omega}{\omega} + \alpha\frac{\rho}{\mu_t}P_k - \beta\rho\omega^2\right. \tag{4}$$

$$l_{IDDES} = \widetilde{f}_d(1+f_e)\cdot l_{RANS} + (1-\widetilde{f}_d)\cdot l_{LES} \tag{5}$$

where k is the turbulence kinetic energy, ω is the dissipation rate, $\vec{u}$ is the fluid velocity vector. μ is the dynamic viscosity. μ_t is the turbulence viscosity, P_k is the production term in the solution process, and F_l, α, σ_ω, σ_k, $\sigma_{\omega 2}$, are constants. l_{RANS} is the turbulence length scale of RANS, l_{LES} is the turbulence length scale of LES. $\widetilde{f}_d$ is an empirical function mainly used for transitioning from the RANS model to scale-resolved model, f_e is a lifting function designed to prevent a significant reduction in Reynolds stress in the near-wall region during the transition process (Yang et al., 2024a,b).

2.2. FWH acoustic analogy

The FW-H acoustic analogy equation precisely reorganizes the con-

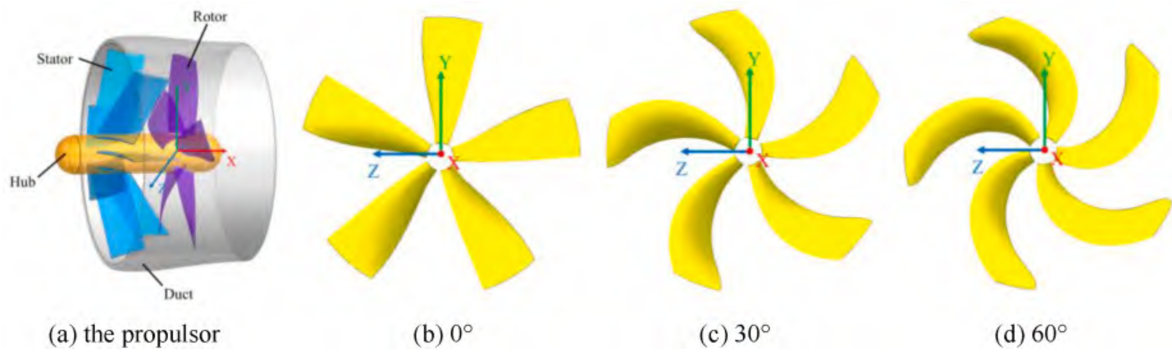

Fig. 1. Geometry of rotor blade skew angle.

Table 1
Operating condition.

D_R (m)	n (rps)	V_a (m/s)	J
0.322	7	1.8032	0.8

tinuity and momentum equations into a form of the non-homogeneous wave equation, and its form is as follows:

$$\left(\frac{\partial^2}{\partial t^2}-c_0^2\frac{\partial^2}{\partial x_i^2}\right)\rho' = \frac{\partial}{\partial t}\left\{[\rho(v_i-u_i)+\rho_0 v_i]\delta(f)\frac{\partial f}{\partial x_i}\right\} - \frac{\partial}{\partial x_i}\left\{\left[\rho v_i(v_j-u_j)+P_{ij}\right]\delta(f)\frac{\partial f}{\partial x_j}\right\}+\frac{\partial^2}{\partial x_i\partial x_j}\{T_{ij}H(f)\} \tag{6}$$

Based on the FW-H equation, its integral form by free space Green's function can be expressed as follows (Xie et al., 2025), consisting of the monopole term p'_T, the dipole term p'_L (Farassat et al., 1980), the quadrupole term p'_Q (Siemens, 2023):

$$4\pi p'_T(x,t)=\frac{\partial}{\partial t}\int_S\left[\frac{Q}{r(1-M_r)}\right]_{ret}dS \tag{7}$$

$$4\pi p'_L(x,t)=-\frac{\partial^2}{\partial x_i}\int_S\left[\frac{L_i}{r(1-M_r)}\right]_{ret}dS \tag{8}$$

$$4\pi p'_Q(x,t)=\frac{\partial^2}{\partial x_i\partial x_j}\int_V\left[\frac{T_{ij}}{r(1-M_r)}\right]_{ret}dV \tag{9}$$

where $p'=p'_T(x,t)+p'_L(x,t)+p'_Q(x,t)$,it is the sound pressure. $Q=\rho_0\left[\left(1-\frac{\rho}{\rho_0}\right)v_i+\frac{\rho}{\rho_0}u_i\right]n_i$.

$L_i=[(p-p_0)\delta_{ij}-\sigma_{ij}]n_i+\rho u_i(u_n-v_n)$, $T_{ij}=\rho u_i u_j+\delta_{ij}[(p-p_0)-c_0^2(\rho-\rho_0)]-\sigma_{ij}$. ρ_0 is the far-field fluid density, ρ is the fluid density. $P_{ij}=(p-p_0)\delta_{ij}-\sigma_{ij}$, it is the compressive stress tensors, $H(f)$ is the Heaviside function. δ_{ij} is the Kronecker symbol, σ_{ij} is the viscous stress tensor, T_{ij} denotes the Lighthill stress tensor, c_0 is the speed of sound in the fluid. $v_n=\vec{v}\cdot\vec{n}$, $\vec{v}$ is the velocity vector of the moving surface, and $\vec{n}$ is the unit normal vector pointing from the object surface towards the fluid. $u_n=\vec{u}\cdot\vec{n}$, $\vec{u}$ is the velocity vector of fluid. $M_r=\vec{M}\cdot\hat{r}$, $\hat{r}$ is the unit vector from a point on the object surface to the observer, $\vec{M}=\vec{v}/c_0$. The subscript "ret'' means that variables inside the square brackets are computed at the corresponding retarded time.

2.3. Noise source extraction and simplification

Based on the FW-H equation, Farassat et al. (2007) derived its integral solution, known as the Farassat 1 A formula, the integration surface can be divided into permeable and impermeable surfaces. When the permeable surface coincides with the object surface, i.e., when the integration surface is the surface of a solid body in the fluid, it corresponds to the integral solution for the impermeable surface. The formulas for the monopole term p'_T, and dipole term p'_L (Brentner et al., 1998) are as follows:

$$4\pi p'_T(x,t)=\int_{f=0}\left[\frac{\rho_0\dot{v}_n}{r(1-M_r)^2}+\frac{\rho_0 v_n\hat{r}_i\dot{M}_i}{r(1-M_r)^3}\right]_{ret}ds+\int_{f=0}\left[\frac{\rho_0 c v_n(M_r-M^2)}{r^2(1-M_r)^3}\right]_{ret}ds \tag{10}$$

$$4\pi p'_L(x,t)=\int_{f=0}\left[\frac{\dot{p}\cos\theta}{cr(1-M_r)^2}+\frac{\hat{r}_i\dot{M}_i p\cos\theta}{r(1-M_r)^3}\right]_{ret}ds+\int_{f=0}\left[\frac{p(\cos\theta-M_i n_i)}{r^2(1-M_r)^2}+\frac{p\cos\theta(M_r-M^2)}{r^2(1-M_r)^3}\right]_{ret}ds \tag{11}$$

where $\cos\theta=\vec{n}\cdot\vec{r}$, θ is the local angle between normal vector $\vec{n}$ to the surface and radiation direction vector $\hat{r}$. $M_i=v_i/c_0$. $\hat{r}_i$ is the component of $\hat{r}$.

Currently, research on near-field sound sources primarily focuses on the extraction and analysis of the dipole and quadrupole sound source characteristics (Yu et al., 2025a,b; Hu et al., 2022; Kojima et al., 2023; Turner et al., 2022). Based on the studies of Yu et al. (2025a,b)Özden et al. (2016), and Cianferra et al. (2019),this study extracted p and $\dot{p}$ from equation (11) as the characterization of the dipole sound source, and extracted the $\frac{\partial^2 T_{ij}}{\partial x_i\partial x_j}$ from equation (9) as the characterization of the quadrupole sound source. These were used to analyze the distribution of dipole and quadrupole sound sources on the surface of the solid body and in the wake field. In this study, T_{ij} is not simplified to $\rho u_i u_j$, it in equation (9) is directly used.

3. Verification and validation

3.1. Geometric model

In this paper, the components of the PJP are shown in Fig. 1(a), where the stator has 7 blades, the rotor has 5 blades, the blade airfoil shape is NACA 66. The axial length of the duct is 0.225 m, and the tip clearance between the rotor blade tip and the inner wall of the duct is 1 mm. Three rotor skew angles are investigated: 0°, 30°, 60°, in the subsequent analysis, these cases are denoted as Case 1, Case 2, and Case 3, respectively, with the geometric schematics shown in Fig. 1(b), (c), (d). The rotor diameter $D_R=0.322$ m, and the advance ratio $J=0.8$, the operating condition is shown in Table 1.

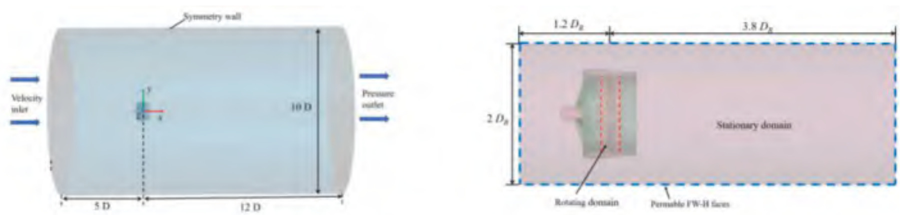

(a) Calculation domain and boundary conditions (b) Acoustics calculation domain

Fig. 2. Calculation domain and setup.

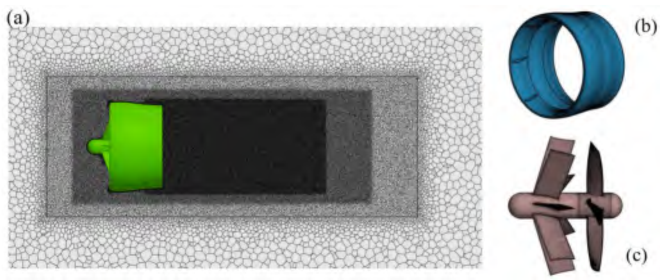

Fig. 3. Computational mesh.

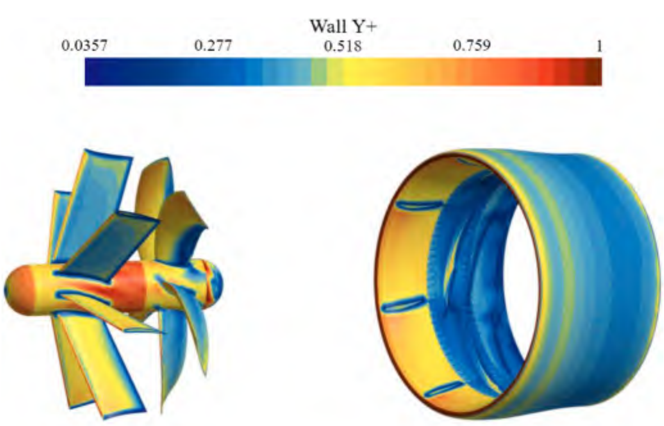

(a) Rotor and stator (b) Duct

Fig. 4. Distribution of y^+ value of PJP surface.

3.2. Computational domain and mesh

Considering the complexity of the research and computational efficiency, the computational domain is established in the commercial software STAR-CCM+, version 2302. As referenced from Li et al. (2025), the entire computational domain was modeled as a cylinder with a diameter of 10 D_R, inlet boundary located 5 D_R away from the propulsor and the outlet boundary positioned at 12 D_R. The inlet boundary condition was set as velocity inlet, and the outlet boundary condition was set as pressure outlet, the surrounding walls were defined as symmetry wall, as shown in Fig. 2(a).

In the FW-H acoustic analogy method, the integration surface for obtaining sound pressure data can be divided into two types: impermeable and permeable surfaces. The impermeable surface typically refers to the surface of the object, where the integration is performed over the physical surface. The permeable surface, on the other hand, is an integration surface that encloses the entire object externally. The term "permeable" here does not have a real physical meaning but is rather a mathematical concept, allowing quantities such as velocity and pressure to pass through this surface. In contrast, "impermeable" generally has a real physical meaning, referring to the solid surface of the object.

The use of a permeable FW-H integration surface allows for the acquisition of nonlinear quadrupole sound pressure data, and this method has been widely applied. For a propulsor, which is a rotating machinery, the permeable surface is generally a regular cylindrical shape. Based on the study by Qin et al. (2019), the size of the permeable integration surface in this paper is shown in Fig. 2 (b). To effectively capture a larger amount of nonlinear sound sources, the diameter of the 'integration surface is set to 2 D_R, with its axis aligned with the rotor's rotation axis, the total axial length of the integration surface is 5 D_R.

Based on the study by Yang et al. (2024), this paper also adopted a similar multigrid refinement strategy, as shown in Fig. 3(a), while a polyhedral mesh strategy was used in this study. Considering computational efficiency, some studies (Porcacchia et al., 2025; Zhang et al., 2022) primarily refine the mesh in the rotor tip and hub regions. In order to capture the quadrupole noise sources as accurately as possible, this paper refined the mesh over the entire wake flow field region. Refinement was also particularly focused on the surface of duct, stator, rotor, and hub. The basic size of the grid is 0.5% D_R m (1.6×10^{-3} m), while the rotor edge features a finer grid size of 2×10^{-5} m. To ensure that the y^+ values on the PJP surface are as small as possible and consistently below 1, the first layer of the grid adjacent to the rotor is 5×10^{-6} m, with a normal-direction growth rate of 1.2, comprising 28 layers. The y^+ distribution on the surface of the PJP is shown in Fig. 4, which meets the computational requirements, ensuring adequate resolution of viscous bottom layer flow.

3.3. Numerical setup

In this study, the rotor operated at a fixed rotation rate of 7 rps. The turbulence model was IDDES, and the finite volume method was used to discretize the control equation system. The pressure term was discretized using a second-order discretization format, and the upwind scheme was second-order. The pressure–velocity coupling based on the SIMPLE algorithm was used (Yang et al., 2024a,b). The *SST k-ω* model was first used for 2000 steps of steady state calculations. To improve computational efficiency, the time step size was set to 0.0007936 s (the time for the rotor to rotate 2°) for transient calculations over a total of 10 cycles, in order to obtain a stable initial flow field. The time step size was then set to 0.0001984 s (the time for the rotor to rotate 0.5°) for transient calculations over a total of 16 cycles. The inlet flow velocity (V_a) is set to 1.8032 m/s, the rotational velocity at the rotor blade tip is 7.0811 m/s, therefore, the actual velocity is: $v = \sqrt{7.0811^2 + 1.8032^2} \approx 7.306\, m/s$, the Courant Friedrichs Lewy (CFL) number $CFL = u\frac{\Delta t}{\Delta x} = 7.306 \times \frac{0.0001984}{0.0016} \approx 0.90 < 1$, could guarantee the stability in the numerical calculations.

3.4. Mesh convergence study

In order to ensure the validity of the mesh, a mesh uncertainty analysis was performed. Three different mesh sizes, coarse, medium, and fine were used in this study, with a mesh size variation rate of $\sqrt{2}$. In this study, Case 2 was calculated under the operating condition of $J = 0.8$

Table 2
Grid number in different domains (unit: Millions).

Mesh	Rotating domain(M)	Static domain(M)	Total(M)
fine	10.93	50.16	61.09
medium	6.75	19.56	26.31
coarse	3.88	7.82	11.70

Table 3
Numerical simulation results.

Mesh	K_T	$10K_Q$	η
fine	0.7083	1.5312	0.5889
medium	0.7110	1.5426	0.5868
coarse	0.7159	1.5597	0.5844

Table 4
Grid uncertainty analysis.

Item	R	φ_{ext}^{21}	e_a^{21}	e_{ext}^{21}	GCI_{fine}^{21}
K_T	0.5551	0.7049	0.39%	0.48%	0.6%
$10K_Q$	0.6668	1.5084	0.74%	1.51%	1.86%
η	0.8673	0.6027	0.35%	2.28%	2.92%

(Table 1). Considering that repeated adjustment of the mesh parameters for grid generation requires considerable effort, and that performing additional numerical calculations with the modified meshes entails substantial computational cost, an efficient computational strategy was adopted. Specifically, the time step was set to the time corresponding to a rotor rotation of 2°, and the results averaged over the last revolution were used for the analysis. The numbers of mesh elements in different regions are shown in Table 2, and the calculation results for different mesh schemes are provided in Table 3. This paper primarily performed a grid independence analysis on three parameters: the total thrust coefficient K_T, the rotor torque coefficient 10 K_Q, overall efficiency η. Other parameters, including the rotor thrust coefficient K_{Tr}, the duct thrust coefficient K_{Td}, the stator thrust coefficient K_{Ts}, the rotor torque coefficient K_Q would be analyzed in the subsequent sections. These coefficients are defined as follows:

$$J = \frac{V_a}{nD_R}, K_{Tr} = \frac{T_r}{\rho n^2 D_R^4}, K_{Ts} = \frac{T_s}{\rho n^2 D_R^4},$$

$$K_{Td} = \frac{T_d}{\rho n^2 D_R^4}, K_T = K_{Tr} + K_{Ts} + K_{Td}$$

$$10K_Q = \frac{10Q}{\rho n^2 D_R^5}, \eta = \frac{J}{2\pi}\frac{K_T}{K_Q}$$

where V_a refers to the flow velocity, n denotes to the rotational speed. D_R is the diameter of the rotor, T_r and Q denote the thrust and torque of the rotor. T_d denotes the thrust of the duct. T_s is the stator thrust. T represents the thrust of the total.

Following Celik et al. (2008), the Grid Convergence Index (GCI) method was applied to perform the mesh uncertainty analysis in this study. This method provides the convergence rate R, the extrapolation values φ_{ext}^{21}, the relative errors e_a^{21}, the extrapolation errors e_{ext}^{21}. The fine grid convergence index GCI_{fine}^{21} was also evaluated, with the results presented in Table 4. When $0 < R < 1$, convergence is observed. The values of e_a^{21} for these three coefficients are all within 1%, which suggests that the grid and numerical methods are reasonable. The maximum extrapolation errors e_{ext}^{21} is 2.28%, which is less than 2.5%; and the maximum GCI_{fine}^{21} is 2.92%, which is less than 3%. Overall, the current grid scheme exhibits good convergence to a certain extent, considering both computational resources and efficiency, the medium grid scheme was adopted for the subsequent numerical calculations.

To verify the reliability of the numerical method, open water performance tests were conducted on the pump-jet propeller, and the numerical simulation results were compared with the experimental values, as shown in Fig. 5. The experiment (Su et al., 2026) was conducted in the towing tank of the Ship and Ocean Engineering Experiment Centre at Shanghai Jiao Tong University. The towing tank is 300 m long, 16 m wide, and 7.5 m deep, and is equipped with a high-speed carriage with a maximum speed of 10 m/s, as shown in Fig. 5 (a). The open-water test was conducted using an open-water box. The PJP was mounted at the top of the shaft tube of the open-water box, and the top of the box was connected to the towing carriage. The driving motor was installed inside

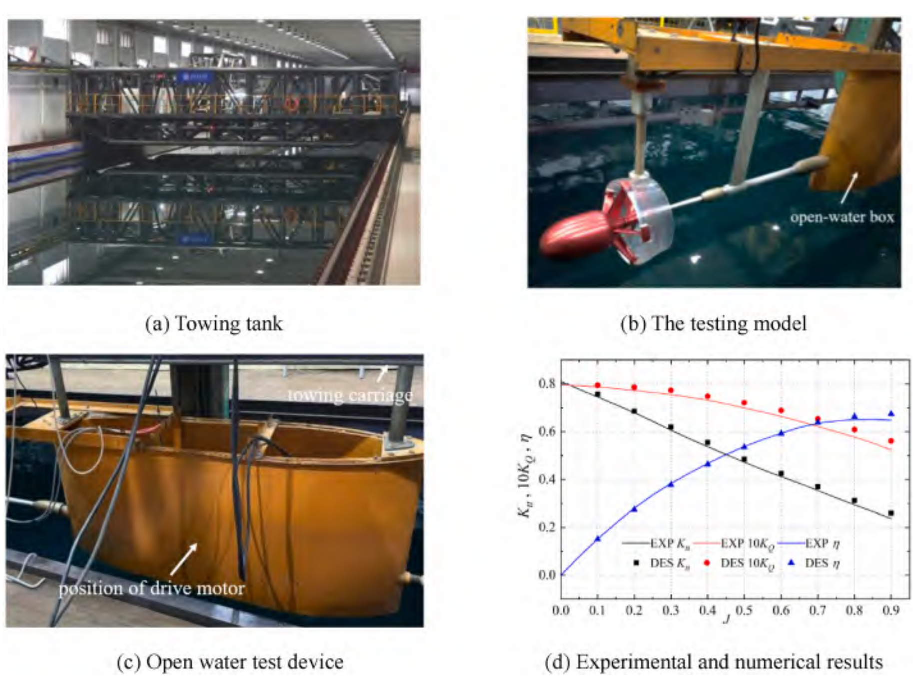

Fig. 5. Open water test arrangement and results.

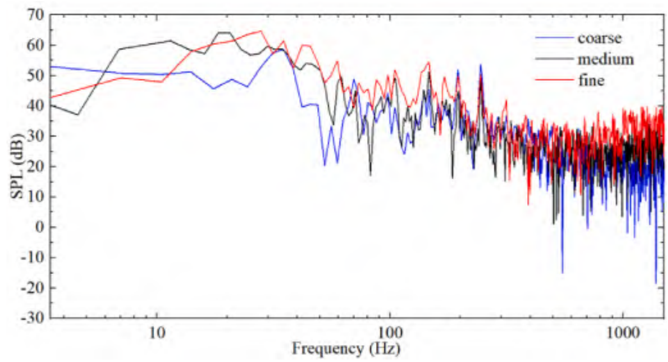

Fig. 6. Spectrum distribution corresponding different grid schemes.

Table 5
Hydrodynamic coefficients: the average values of last two cycles.

	K_T	K_{Tr}	K_{Td}	K_{Ts}	$10K_Q$	η
Case 1	0.4909	0.4524	0.1157	−0.0773	1.1022	0.5671
Case 2	0.7121	0.6122	0.1998	−0.0999	1.5432	0.587
Case 3	0.452	0.4165	0.117	−0.0814	0.9614	0.5987

the box. During the test, the rotor rotational speed was kept constant, while the advance speed was varied.

For different advance ratios J, the relative error in efficiency η remains within 3.1%, the relative error for K_{tt} and 10 K_Q are within 5%, except at the high advance coefficient $J = 0.9$, the max relative error for K_{tt} and $10K_Q$ are 8.6% and 7.1%. Overall, the errors fall within engineering permissible error ranges (X. Huang et al., 2022).

To assess the reliability of acoustic results for the current grid scheme, the spectral distribution at the same lateral noise monitoring point for three schemes of grids are shown in Fig. 6, with the coordinates being (0, 100 D_R, 0). Overall, the spectral distribution curves corresponding to the three types of grids are relatively close, with no significant differences. There are some differences in the low-frequency and high-frequency distributions, which may be related to the ability of the grid size to resolve the vortex structures.

4. Results and discussion

4.1. Skew effects on hydrodynamic performance

The hydrodynamic coefficients corresponding to different rotor angles are shown in Table 5, with the values taken as the average of the last two cycles. As the skew angle increases, the efficiency η also gradually increases. However, for the other coefficients, the trend first increases and then decreases. Case 2 appears to be a turning point, at which K_T,

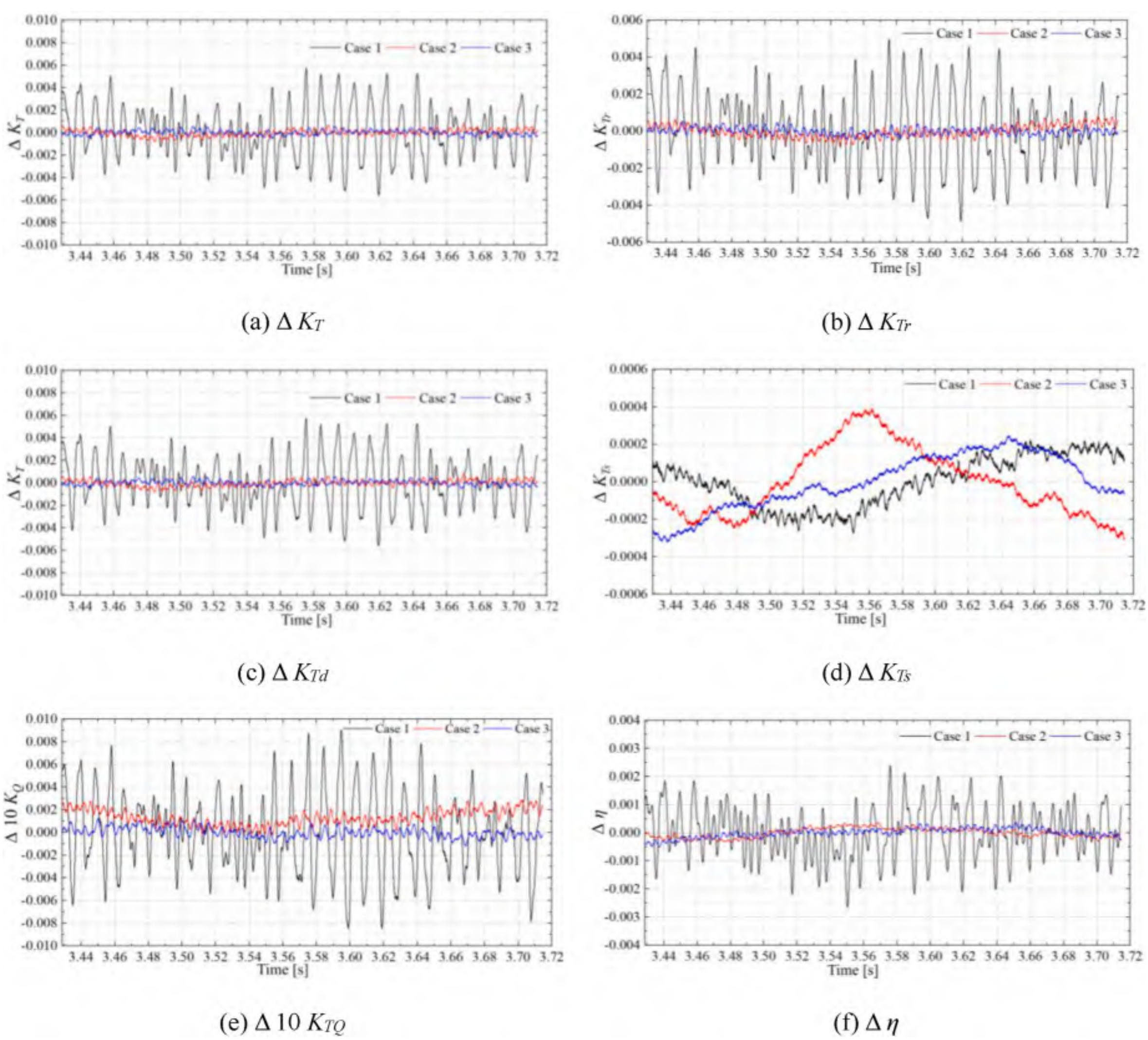

Fig. 7. Fluctuations of unsteady force: coefficients have been offset to have a zero-mean value.

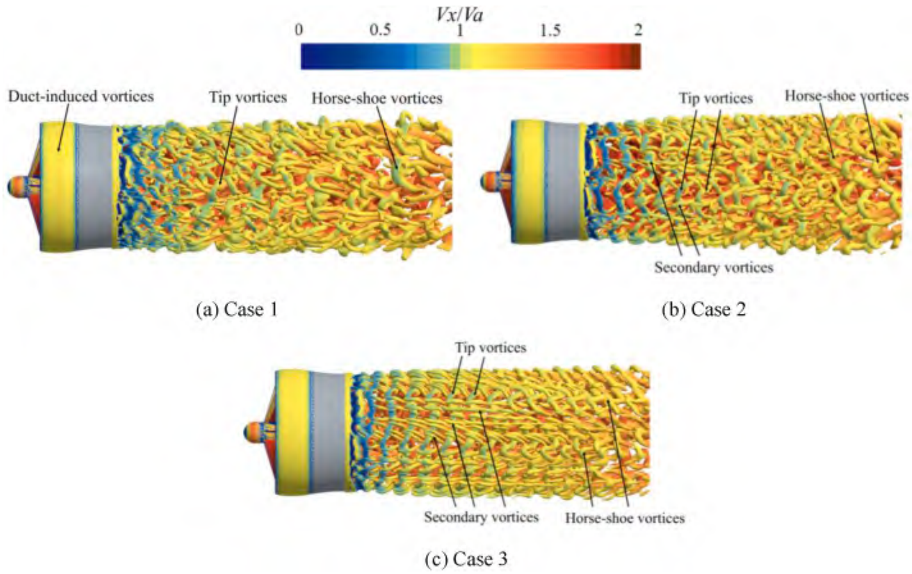

Fig. 8. Instantaneous Q surfaces (Q = 200 s^{-2}).

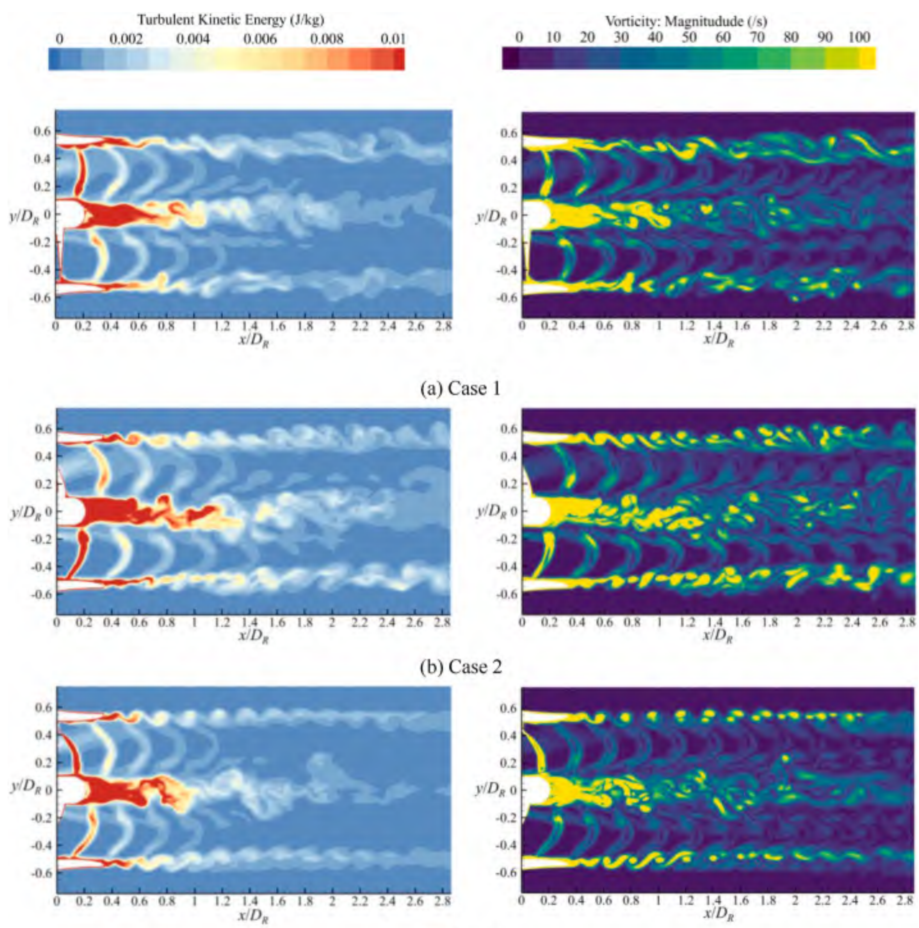

Fig. 9. Flow field analysis in the x–y plane.

K_{Tr}, K_{Td}, K_T and $10K_Q$ all reach their maximum values. From the efficiency perspective, under the working conditions studied in this paper, simply increasing the skew angle leads to a gradual increase in efficiency.

From an engineering perspective, Case 2 provides a more balanced hydrodynamic performance because it yields the highest K_T, while maintaining a relatively high efficiency. Compared with Case 2, Case 3 improves the efficiency by only 2%, but causes a 36.53% loss in thrust. Such a thrust loss appears to be an unfavorable trade-off for only a 2% improvement in efficiency. Case 3 may be more suitable for operating

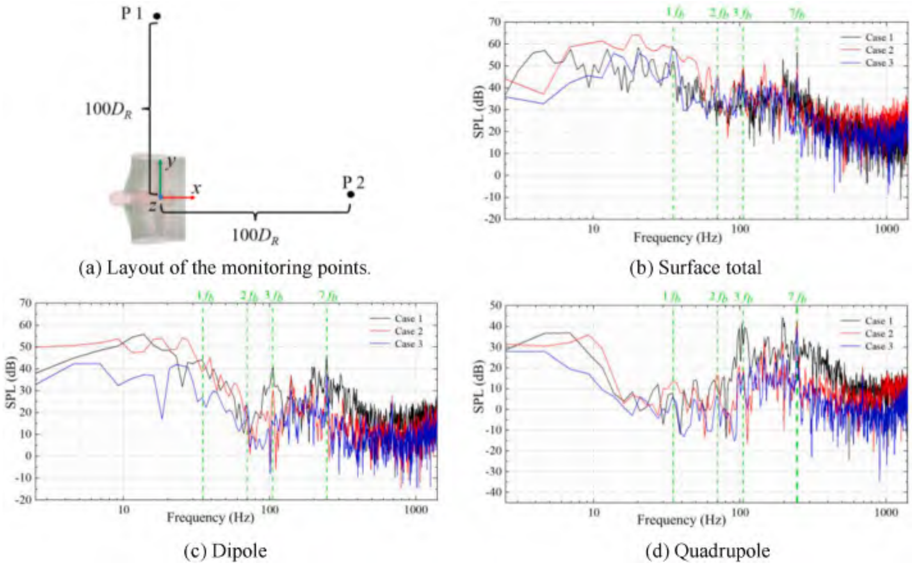

Fig. 10. Spectrum analysis of sound pressure at P 1.

Table 6
OASPL values at different monitoring points.

	P 1 (dB)			P 2 (dB)		
	Surface total	Dipole	Quadrupole	Surface total	Dipole	Quadrupole
Case 1	70.01	60.6	18.84	73.55	52.81	16.51
Case 2	70.92	61.39	11.29	69.99	48.91	10.18
Case 3	63.63	49.96	8.31	60.44	41.34	8.63

conditions where lower thrust and potentially lower noise are prioritized. During the design of a PJP, if the thrust loss associated with a large skew angle needs to be compensated, possible approaches include increasing the rotor rotational speed or further optimizing the blade geometry. However, increasing the rotational speed may also result in higher noise levels. Therefore, the selection of rotor skew angle should depend on the specific design objective and operating scenario rather than solely on the maximum efficiency value.

The fluctuation of the hydrodynamic coefficients over time is shown in Fig. 7. Due to the large differences in the average values of the coefficients corresponding to different skew angles, and because the fluctuation amplitudes (real values minus the average values) are relatively small compared to the real values, directly plotting the real values would make it difficult to clearly display the fluctuations over time for all three skew angles on the same graph. Therefore, this paper chooses to plot the time history curves of the fluctuation values (real values minus the average values).

Overall, for ΔK_T, ΔK_{Tr}, ΔK_{Td}, ΔK_Q and $\Delta \eta$, these parameters exhibit periodic peaks and valleys. However, the peak values for Case 1 (skew angle is 0°) are always higher than those for Case 2 and Case 3, this likely indicates that the skew angle helps distribute the load more evenly on the blade surface, resulting in smoother flow and smaller fluctuations in the hydrodynamic coefficients. In contrast, the periodicity of ΔK_{Ts} is less pronounced and the fluctuation amplitude is smaller, with the maximum value not exceeding 0.0004, much lower than the

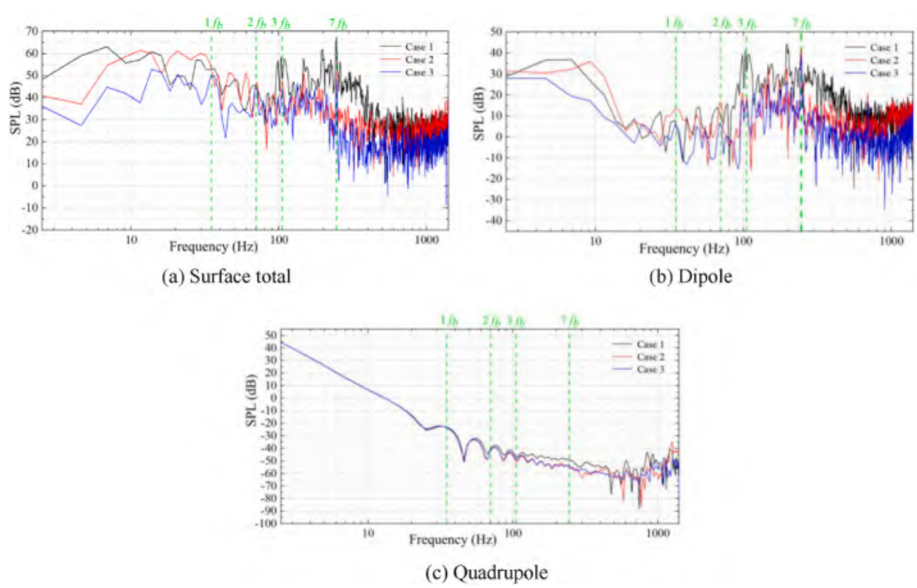

Fig. 11. Spectrum analysis of sound pressure at P 2.

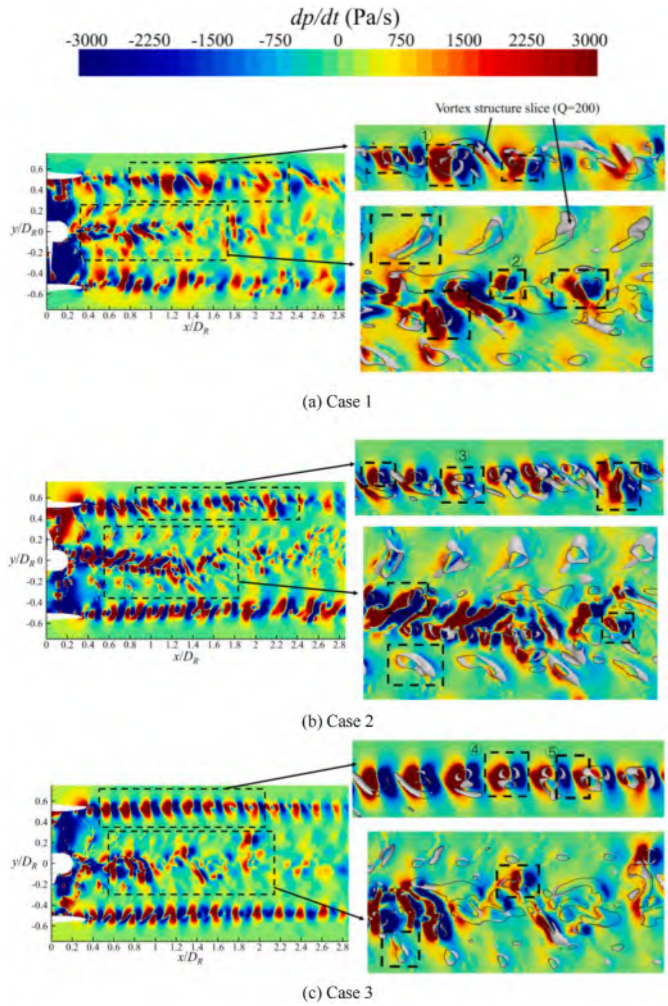

Fig. 12. The dipole source distribution in the x–y plane.

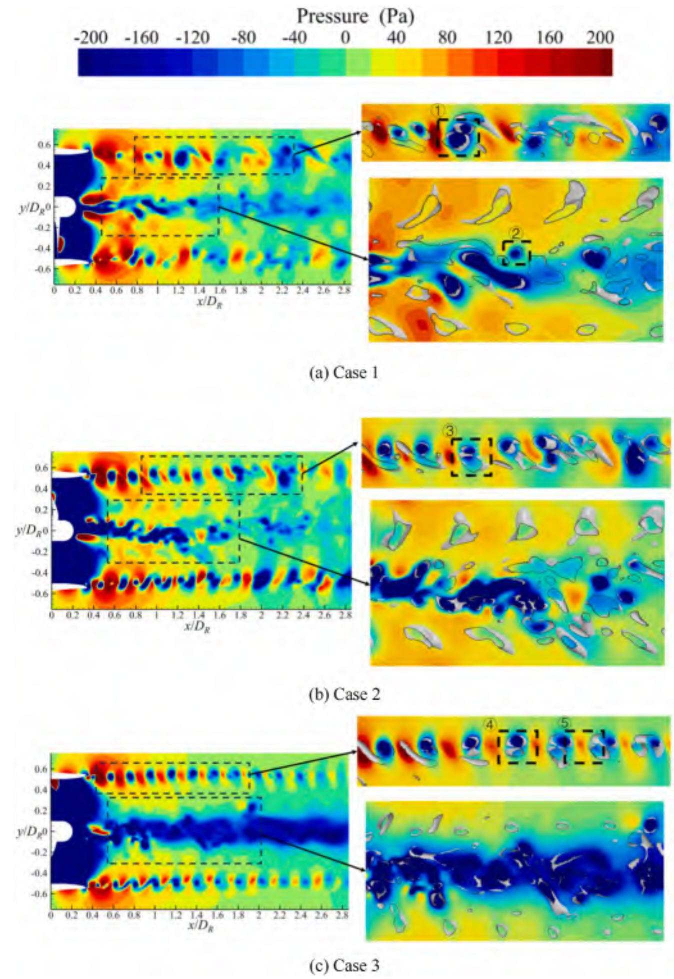

Fig. 13. The pressure distribution in the x–y plane.

peak values of the other parameters. This may suggest that the axial force generated by the stator is less influenced by rotor rotation, and the variation in skew angle has a smaller impact on changes in axial force.

4.2. Flow field analysis

Fig. 8 shows the instantaneous Q surfaces of the PJP. For Case 1, the tip vortices filaments are not standard spiral, as the skew angle increases, the shape of the tip vortices becomes more regular, and the spiral pattern becomes more pronounced. Secondary vortices are vortex structures that develop along the axial direction and have a much smaller diameter compared to the primary vortices. A similar vortex structure was also observed in the study by Q Huang et al. (2022), however, in the present study, as the skew angle increases, the secondary vortices exhibit a gradually more pronounced and stable trend. In Fig. 8(c), the secondary vortex structure for Case 3 is the most pronounced. According to Di Mascio et al. (2014) the secondary vortices play an important role in the destabilization of the tip vortices, when the flow develops downstream to a certain distance, both the secondary vortices and tip vortices disappear. This is likely due to the merging of these two structures, resulting in the formation of a horse-shoe vortex structure.

Overall, the increase in skew angle seems to have a tendency to make the wake field develop more regularly and the flow more stable, specifically, the tip vortices and secondary vortices become more pronounced, stable, and regular, with their spatial extent in the downstream direction increasing as the skew angle increases. Considering the efficiency η from Table 5, a more stable and uniform flow field contributes to an increase in η.

The distribution of Turbulent Kinetic Energy (TKE) and vorticity is shown in Fig. 9. The distribution of TKE shows a certain correlation with vorticity. Near the hub, the distributions of TKE and vorticity are quite pronounced, and the shapes of the distribution areas are similar. However, in the region between the hub and the blade tip, vorticity more clearly reveals the traces of the rotor trailing vortex in the wake, which remain visible even as the wake develops downstream to 2 D_R. In contrast, TKE dissipates more quickly as the wake moves downstream, becoming less distinct beyond 1 D_R .

4.3. Flow noise analysis

To investigate the effect of the skew angle on the far-field flow noise characteristics, the locations of the far-field monitoring points are shown in Fig. 10 (a). Considering the symmetry of the rotational motion in the yOz plane, only one lateral monitoring point, P 1, was selected for the PJP. A second monitoring point, P 2, is placed directly downstream on the axis. The coordinates of P 1 and P 2 are (0, 100 D_R, 0) and (100 D_R, 0, 0) respectively.

When a permeable integration surface is used, the sound pressure obtained on the integration surface consists of the sum of the monopole and dipole contributions, i.e., the linear terms. The quadrupole sound pressure is treated as a separate contribution and represents the nonlinear term. Table 6 summarizes the OASPL values for different acoustic contributions. Here, "surface total" denotes the OASPL computed from the linear surface terms ($p'_T + p'_L$). "Dipole" refers to the

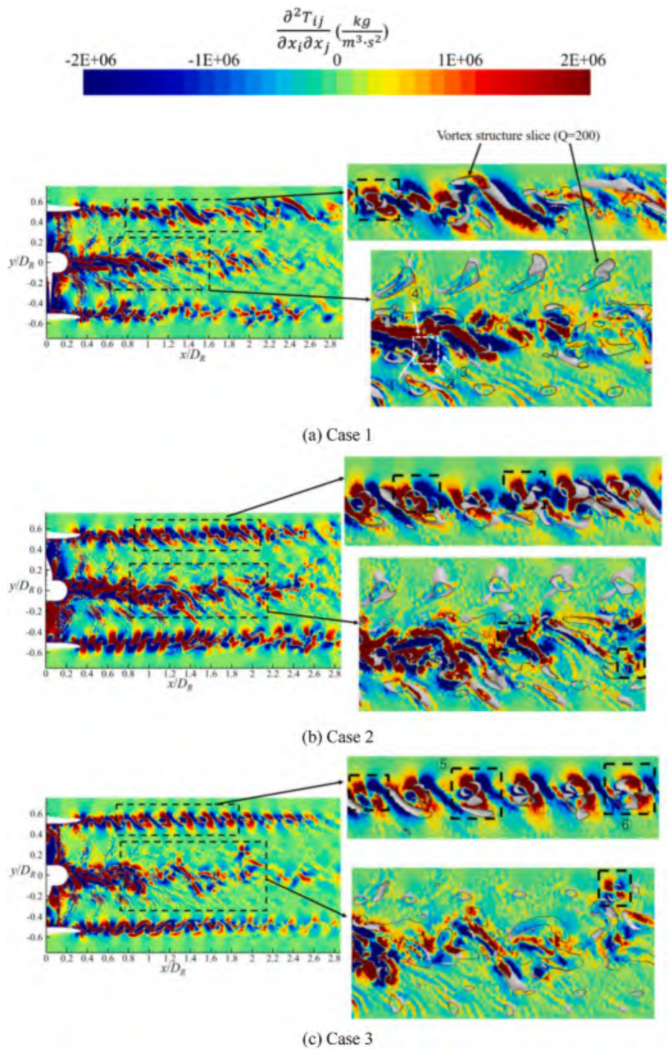

Fig. 14. The quadrupole source distribution in the x-y plane.

OASPL associated with the dipole term (p'_L), whereas "Quadrupole" denotes the OASPL contributed by the quadrupole term. The OASPL can be defined as follows (Xie et al., 2026):

$$SPL = 20\ \lg\ (p / p_0) \tag{12}$$

$$OASPL = 10\ \lg\ \left[\Sigma^N \left(10^{SPL_N/10}\right)\right] \tag{13}$$

where p is the sound pressure, p_0 is the reference sound pressure, which is taken as 1×10^{-6} underwater. N is the number of frequency points within the frequency band, SPL_N is the SPL value corresponding to the N th frequency.

For the lateral monitoring point P 1, the minimum OASPL of the linear terms is obtained in Case 3, whereas Case 2 yields the maximum value, which is 7.29 dB higher than that of Case 3 and 0.91 dB higher than that in Case 1. This may indicate that, for the present blade geometry, varying only the skew angle may lead to an initial increase and subsequent decrease in OASPL values, with a possible turning point near 30°. One possible reason maybe that, for same monitoring point located in the lateral direction, the rotor configuration in Case 2 may intensify the interaction between vortex structures and the inner wall of the duct, thereby enhancing pressure fluctuations and increasing the OASPL values. Nevertheless, this result may suggest that, during the design of PJP configurations, increasing the skew angle does not necessarily result in a continuous decrease in OASPL values for certain blade geometries and advance ratios. Instead, a turning point may occur in the variation of OASPL with skew angles.

In contrast, the OASPL associated with the quadrupole contribution decreases monotonically with increasing skew angles. This trend is likely related to the evolution of the flow field: as discussed in Section 4.2, increasing the skew angles tends to produce a more uniform and stable wake, thereby reducing the quadrupole-source OASPL.

For the downstream monitoring point P 2, the OASPL values of both the linear and nonlinear contributions decrease with increasing skew angles. The linear-term OASPL is reduced by up to 13.11 dB, while the nonlinear (quadrupole) contribution decreases by up to 7.88 dB. These results indicate that the downstream flow-noise OASPL is highly sensitive to variations in the rotor skew angles. Overall, the OASPL of the quadrupole contribution is 52~59 dB lower than that of the surface total (linear) contribution, although its maximum value still approaches 19 dB. For monitoring points at different azimuthal locations, increasing the skew angles consistently leads to a reduction in the quadrupole term OASPL.

As indicated by the spectral results in Figs. 10 and 11, the linear contribution exhibits tonal features at multiple blade-passing frequencies ($2\,f_b$, $3\,f_b$, $7\,f_b$), whereas the component at 1 BPF is less distinct, this may be associated with the use of a permeable integration surface and its size. Building on the studies of Qin et al. (2019), Li et al. (2025) and Zheng et al. (2024), we note that these studies also adopted a permeable integration surface to compute the PJP noise, and in their results, the peaks at 1 BPF are similarly not very distinct. One possible explanation is that the presence of the duct in the PJP affects the development of rotor-induced vortex structures, which in turn alters the pressure field in the flow and consequently influences the integration results obtained from the permeable surface. As the skew angle increases, the dipole noise spectra show a clear reduction: for Case 3, the SPL is lower than that of Case 1 over most of the low-frequency range (0~140 Hz), and this trend holds for nearly the entire frequency range above 140 Hz as well. These results suggest that increasing the skew angle may effectively mitigate dipole-dominated noise.

For the quadrupole contribution, the SPL decay curves for the three skew angles almost coincide in the 0~20 Hz range. This may be because variations in skew angle have a limited influence on low-frequency, large-scale turbulent structures (e.g., shaft-order components such as 7 and 14 Hz). Since quadrupole noise is closely associated with the fluid motion itself, the spectral decay trends of the three cases remain very similar at low frequencies. In the 20~300 Hz range, the amplitude distribution of the spectral curves generally follows the order follows the ordering Case 1 >Case 2 >Case 3, and the overall fluctuation patterns are also similar. This suggests that, within approximately the 3~8 BPF band, increasing the skew angle can reduce quadrupole-dominated noise, and this reduction is observed for both the lateral and downstream directions.

4.4. Sound source analysis

The distribution of dp/dt on the mid-longitudinal plane of the wake is shown in Fig. 12. An enlarged view is provided, in which a Q criterion slice is superimposed to characterize the vortex structures and to examine the relationship between the sound sources and the flow field. As is indicated by the black dashed boxes in Fig. 12, the dipole source distribution is strongly correlated with the vortex structures, around an isolated vortex (e.g., region "②") two distinct dipole lobes with alternating positive/negative (red/blue) signatures can be clearly identified on either side of the vortex. Similar dipole patterns are observed in both the hub vortex and tip vortex regions, suggesting that dp/dt can, to some extent, effectively reveal dipole-like features.

Regions" ①"," ③", "④" indicate that when two vortices have not fully merged and only partially intersect, the dp/dt field still exhibits a single dipole-like pattern. It is also worth noting that, although a red–blue dipole signature appears in region" ⑤", no vortex structure is present within this area. This may indicate that the dipole features

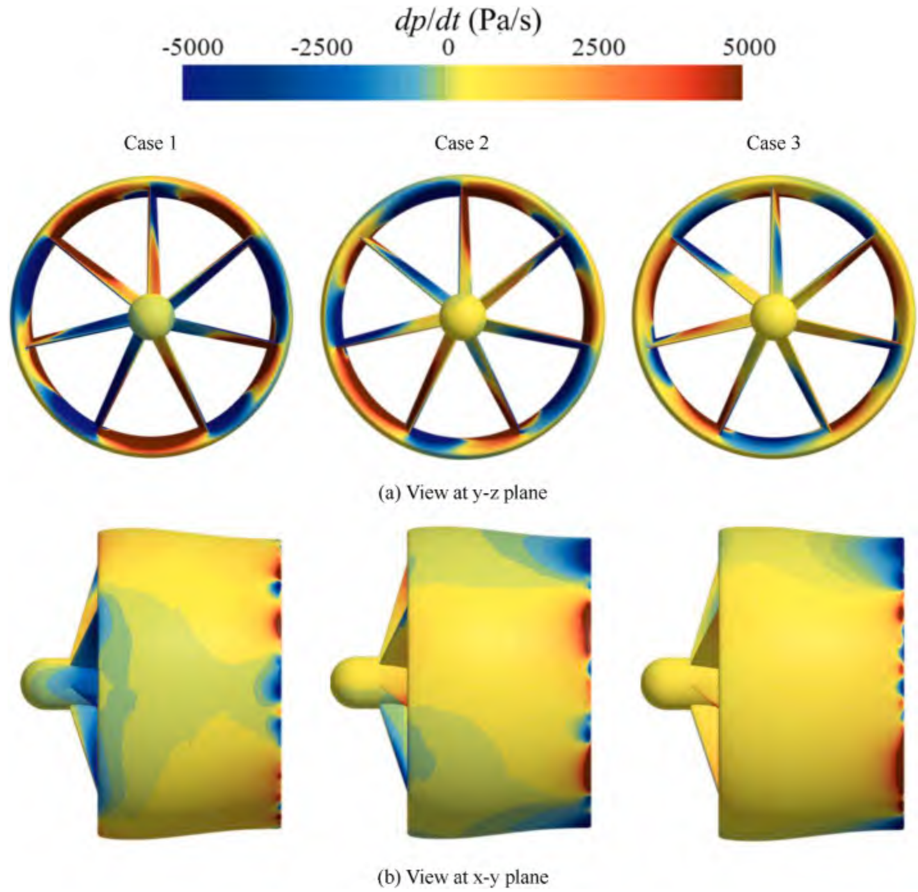

Fig. 15. The dipole source distribution on the duct and stator surface.

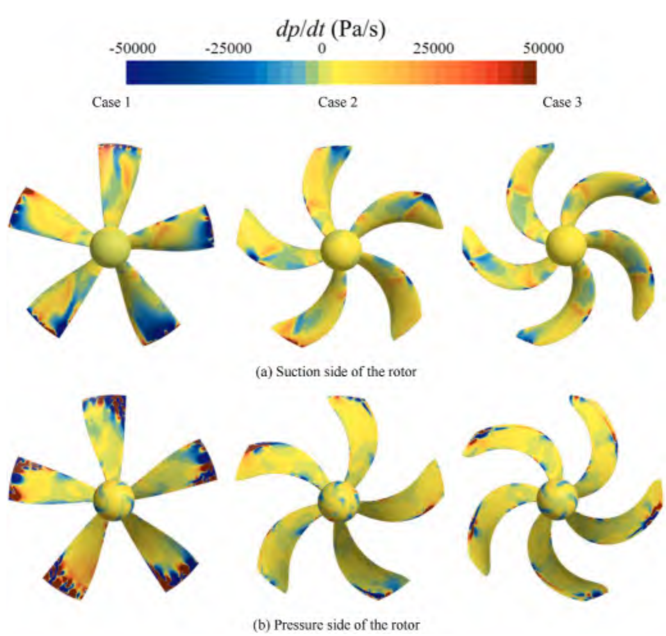

Fig. 16. The dipole source distribution on the rotor surface.

revealed by dp/dt are distributed around the vortex structures.

As discussed in the previous analysis of wake flow field, increasing the skew angle makes the wake structures more regular and uniform. A similar effect is also observed for the dipole sound sources: in Case 3, the distribution in the blade-tip region appears more uniform and more orderly.

Fig. 13 shows the pressure distribution in the same region together with the Q-criterion slice. Compared with Fig. 12, the most notable difference is that the pressure field does not exhibit dipole features. As indicated by the black dashed boxes" ①, ②,③,④", only a low-pressure (blue) region is observed in the vortex-structure areas. In the region between the two vortices ("⑤"),only a single high-pressure region appears.

The distribution of the quadrupole sound sources in the wake on the mid-longitudinal plane is shown in Fig. 14. Around a single vortex slice, a distinct quadrupole pattern can be observed, as indicated by the four arrows labeled "①,②,③,④" in the white dashed box in Fig. 14 (a), four pronounced lobes appear around the vortex core, with alternating red and blue regions and a clear separation between adjacent lobes, making the quadrupole signature readily identifiable. The other black dashed boxes in Fig. 14 also capture this feature well.

However, in regions"⑤,⑥" where two vortices are present but partially intersect, only a single quadrupole feature is observed, similar to the dipole pattern. This may be related to the fact that the two extraction methods have similar limitations in spatial resolution. When the spatial resolution is insufficient, the vortex structures cannot be fully resolved and remain partially merged. For such vortex structures, both extraction methods can still only exhibit a single source characteristic. The influence of spatial resolution on the results obtained by the two extraction methods could be further investigated in future work.

Fig. 15 shows the distribution of dipole sound sources on the duct and stator surfaces. A dipole pattern is observed on the inner wall of the duct in the upstream inflow region, manifested as alternating red and blue patches distributed circumferentially around the inner wall, as shown in Fig. 15 (a). The number of these alternating patches is five, which is consistent with the number of rotor blades, indicating that the

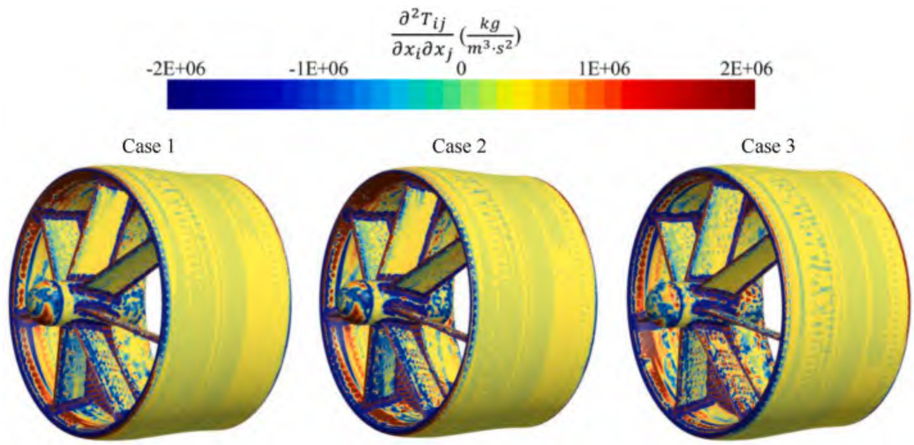

Fig. 17. The quadrupole source distribution on the stator and duct surface.

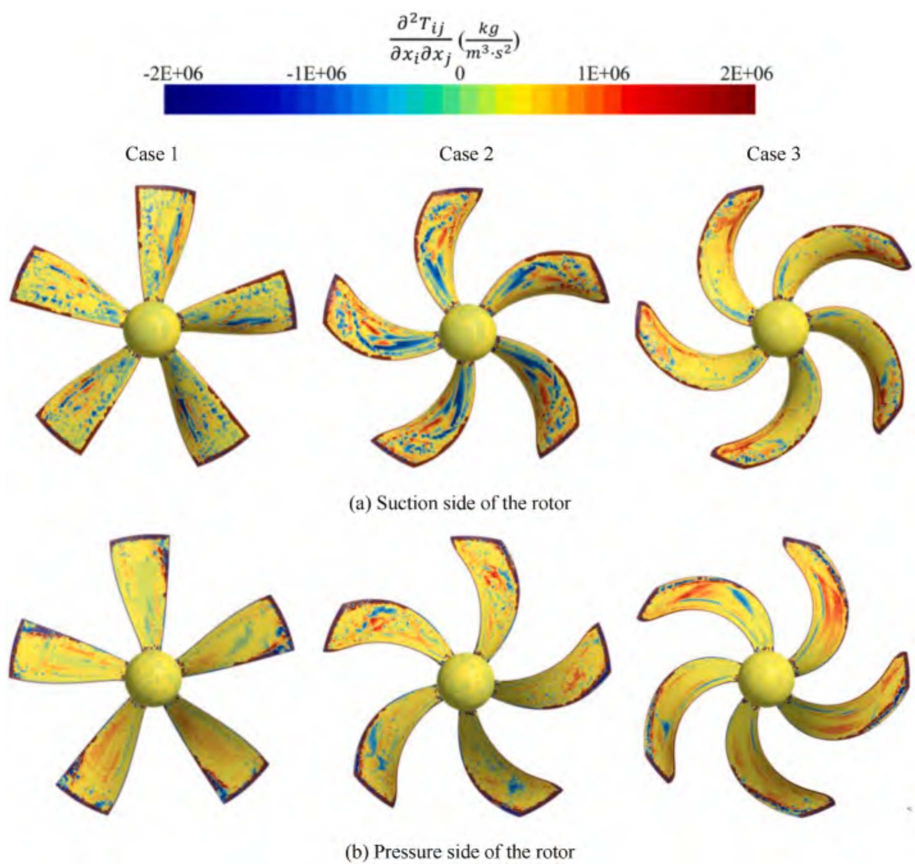

Fig. 18. The quadrupole source distribution on the rotor surface.

pressure fluctuations induced by rotor rotation affect the time derivative of pressure on the duct inner wall. In contrast, in the downstream region on the outer wall of the duct, the dipole source distribution appears to exhibit no strong regularity.

Fig. 16 shows the dipole-source distribution on the rotor surface. Overall, relatively large values of dp/dt are observed near the blade tip, especially on the pressure side of the rotor. On the suction side, the variations of dp/dt near the tip in Case 1 are more pronounced than those in Case 2 and Case 3, indicating that the dipole-source distribution on the rotor surface is less uniform in Case 1. Combined with the effects of skew angle on the hydrodynamic coefficients shown in Fig. 7, increasing the skew angle not only promotes a more uniform load distribution over the blade surface but also improves, to some extent, the uniformity of the dipole-source distribution on the blades.

The distribution of quadrupole sound sources on the duct and stator surfaces is shown in Fig. 17. Overall, relatively large quadrupole-source levels occur near the body boundaries, including the upstream (inflow) region of the duct, the leading- and trailing-edge regions of the stator blades, and the junction between the stator and the duct. Compared with the dipole source distribution, variations in the rotor skew angle have a less pronounced effect on the quadrupole source distribution on the duct wall.

The distribution of quadrupole sound sources on the rotor surface is shown in Fig. 18. The quadrupole sources are particularly pronounced

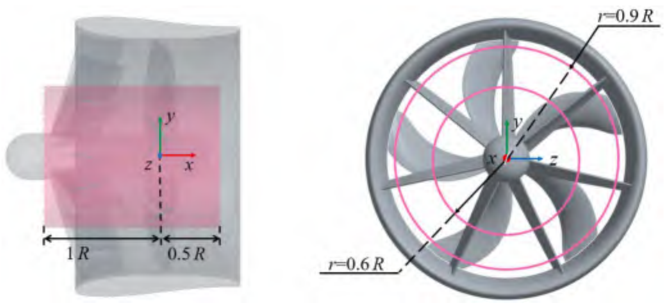

Fig. 19. The cylindrical cut plane.

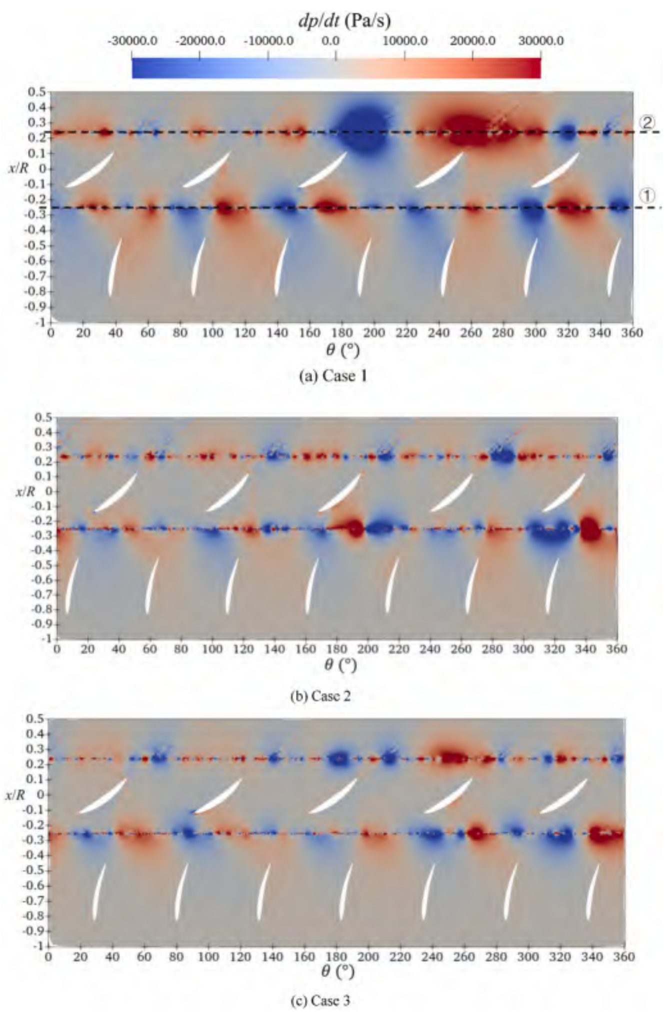

Fig. 20. The dipole source distribution on the cylindrical cut plane at $r/R = 0.6$.

near the blade leading edge, trailing edge, and tip regions, which differs to some extent from the dipole-source distribution. A possible reason is that the Lighthill stress tensor in the quadrupole source term, $T_{ij} = \rho u_i u_j + \delta_{ij}\left[(p - p_0) - c_0^2(\rho - \rho_0)\right] - \sigma_{ij}$, contains the velocity components u_i and the viscous stress tensor σ_{ij}, the presence of a solid wall causes these quantities to exhibit sharp variations at the fluid–wall boundary, leading to more pronounced source levels near the body surfaces. After the flow passes the boundary and the wall-bounded flow becomes progressively more stable, the variations of these quantities become less intense, and the source levels decrease accordingly. This behavior is also observed on the outer duct surface in Fig. 17, where the quadrupole-

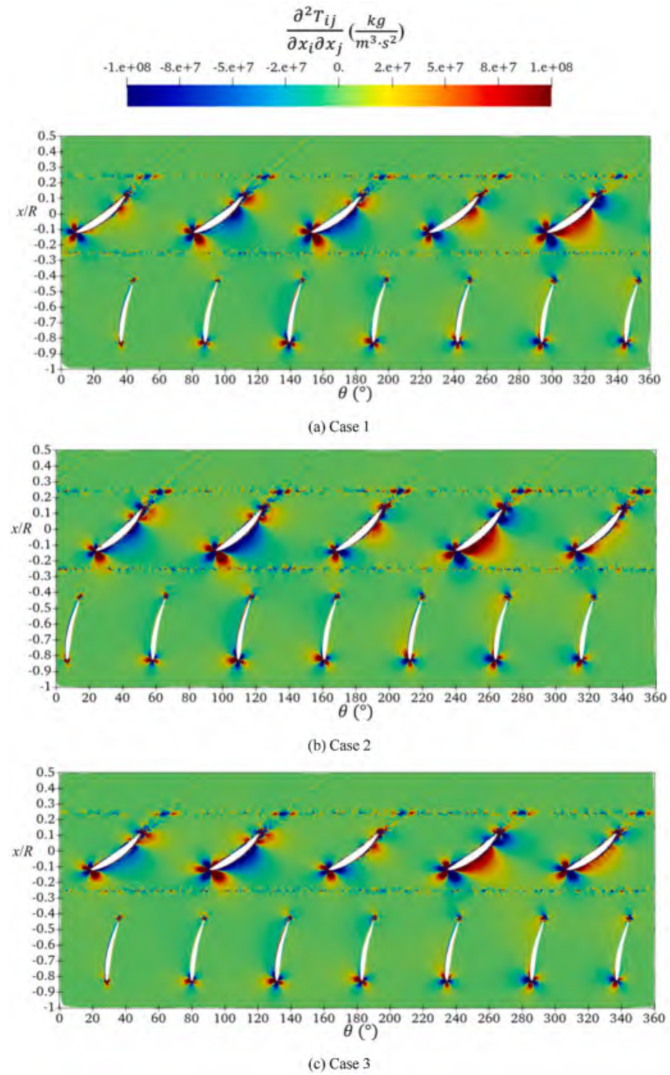

Fig. 21. The quadrupole source distribution on the cylindrical cut plane at $r/R = 0.6$.

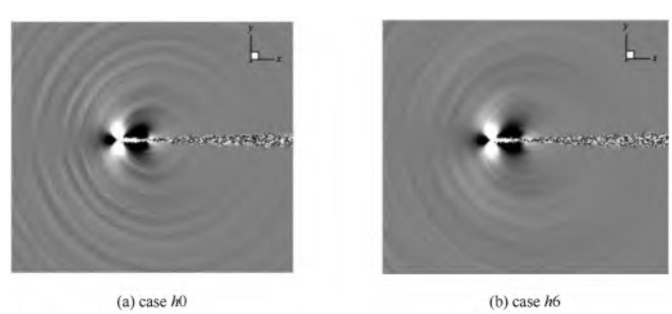

Fig. 22. In the study by Hu et al., the difference between cases (a) and (b) lies in the serration geometry at the airfoil trailing edge.

source levels are relatively small in the mid-span region.

To better analyze the sound-source distribution inside the duct, a cylindrical cut plane is introduced within the duct, and the source distribution on this cut plane is examined. A schematic of the cylindrical cut plane is shown in Fig. 19. The cut plane has a radius of 0.6 R (where R is the rotor radius) and 0.9 R, the axial length is 1.5 R.

The dipole source distribution on the cylindrical cut plane at $r/R = 0.6$ is shown in Fig. 20. In Fig. 20(a) the black dashed line "①"

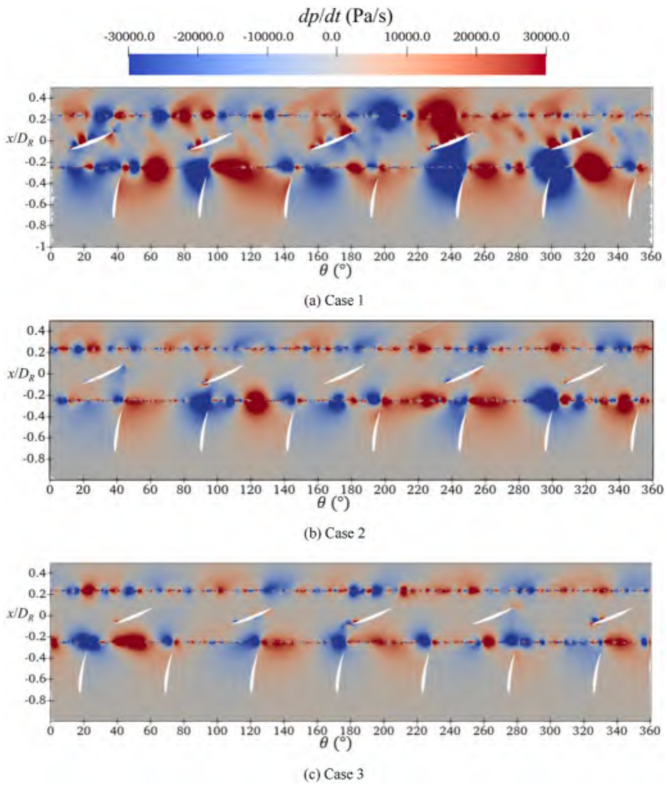

Fig. 23. The dipole source distribution on the cylindrical cut plane at $r/R = 0.9$.

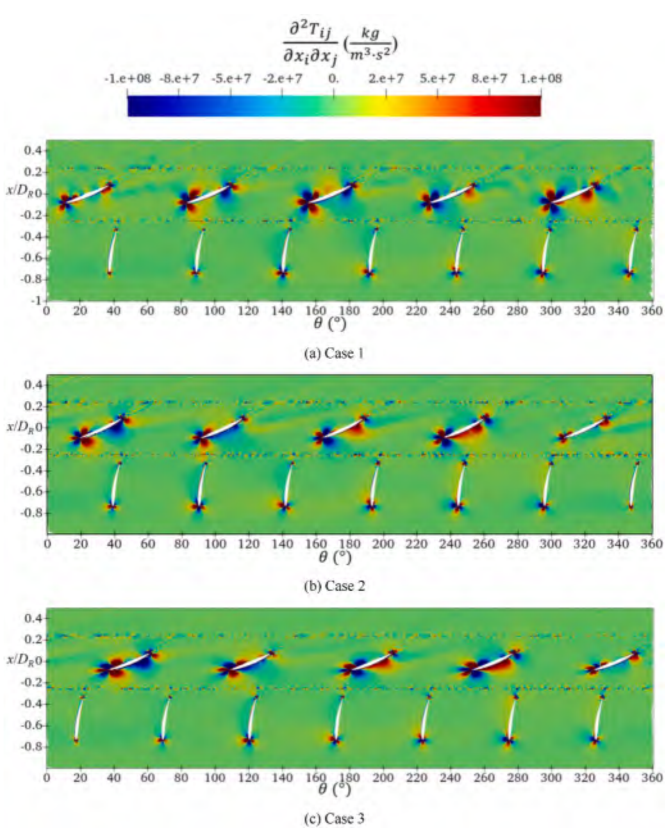

Fig. 24. The quadrupole source distribution on the cylindrical cut plane at $r/R = 0.9$.

denotes the inlet of the rotating–stationary interface between the rotating domain and the stationary domain, and "②" denotes the outlet. It can be seen that dp/dt exhibits relatively strong fluctuations at the interface. From the distribution of the colored patches, Case 1 appears to show the most pronounced features among the three skew-angle cases. In the region downstream of the stator trailing edge and upstream of "①", an evident alternating red–blue pattern is observed, the number of patches of a single color is also five, consistent with the number of rotor blades. This suggests that rotor rotation can also influence the upstream dipole-source distribution.

The quadrupole source distribution on the cylindrical cut plane at $r/R = 0.6$ is shown in Fig. 21. Prominent feature is that clear quadrupole signatures could be observed at the leading edges of both the stator and rotor blades, manifested as four distinct lobes with alternating red and blue regions. This indicates that the quadrupole extraction approach used in this study can capture not only the quadrupole-source characteristics associated with purely fluid motion (as in Fig. 14), but also the quadrupole features induced by moving bodies in the flow. A similar phenomenon was also reported by Hu et al. (2022), as shown in Fig. 22. However, their study was conducted in a gaseous medium and differs from the present work in geometric configuration and acoustic source mechanism. Therefore, for the flow-noise sources underwater, the quadrupole extraction method adopted in this study is effective for qualitative visualization, but it still has some limitations in quantitative analysis and in capturing the detailed acoustic mechanisms.

The dipole and quadrupole source distribution on the cylindrical cut plane at $r/R = 0.9$ shown in Figs. 23 and 24, respectively. Overall, the dipole distribution at $r/R = 0.9$ is similar to that observed at $r/R = 0.6$. However, in Case 1, a more pronounced dipole pattern appears on working side of the rotor blade section. Considering Fig. 16(b), this may be attributed to a less uniform load distribution near the blade tip in Case 1, which results in a stronger dp/dt distribution. In addition, noticeable quadrupole features can be observed along the leading edges of both the stator and rotor blades. This may suggest that the quadrupole extraction method adopted in this study is effective for visualizing flow-induced sound source at different positions within the PJP.

5. Conclusion

In this paper, the flow field of a PJP with 3 different rotor skew angles is simulated. The flow-induced noise is then computed using the FW-H acoustic analogy method to investigate the effects of skew angle on the OASPL and spectral characteristics at the lateral and downstream far-field monitoring points. By extracting and simplifying the acoustic source terms, the influence of skew angles on the interaction between wake vortex structures and acoustic sources is further examined, together with its impact on the distributions of dipole and quadrupole sound sources on the PJP surfaces. The conclusions are obtained as follows:

For the geometric model and operating conditions considered in this study, increasing the rotor skew angle from 0° to 30° and 60°,increases the overall efficiency η by 3.51% and 5.57%, respectively. When the skew angle is 60°, wake flow structures such as the tip vortices and secondary vortices are the most pronounced and persist over a longer downstream distance. Overall, increasing the skew angle tends to make the wake more uniform and stable, thereby promoting an improvement in efficiency.

For the lateral monitoring point, the OASPL of the quadrupole contribution decreases progressively with increasing skew angle, with a maximum reduction of 10.53 dB. For the linear (surface total) contribution, the minimum OASPL occurs at a skew angle of 60°, which is 7.29 dB lower than the maximum value observed at 30°. For the downstream monitoring point, the OASPL of both the linear and nonlinear contributions decrease stepwise as the skew angle increases: the linear contribution is reduced by 13.11 dB, and the nonlinear (quadrupole) contribution is reduced by 7.88 dB. Overall, the skew angle has a pronounced effect on the quadrupole-term OASPL, and increasing the skew angle consistently leads to a reduction in the quadrupole contribution for monitoring points at different directions.

The near-field source analysis of dipole and quadrupole contributions in the wake indicates that using dp/dt to represent the dipole source can reveal clear dipole-like signatures on an isolated vortex tube slice. Likewise, using $\frac{\partial T_{ij}}{\partial x_i \partial x_j}$ to represent the quadrupole source can also exhibit distinct quadrupole-like features on vortex-tube slices. In the wake field, the distributions of dipole and quadrupole sources are largely consistent with the regions of the tip vortex and hub vortex, indicating that vortex structures are an important factor for source identification based on the FW-H acoustic analogy method.

The analysis of sound source on the PJP surface shows that rotor rotation can induce pronounced dipole signatures on the inner wall of the duct, and the number of these features is consistent with the number of rotor blades. The quadrupole sources are particularly evident near the inlet and outlet edges of the duct and around the leading and trailing edges of both the stator and rotor blades, whereas they are much weaker in the intermediate regions. This is likely related to the abrupt variations in the fluid velocity and viscous stress tensor in the Lighthill stress tensor as the flow first comes into contact with the solid wall.

Since the development and dissipation of vortex structures in the wake flow field have an important influence on flow-induced noise, future related work could focus on modal analysis of the coupling between wake vortex dynamics and sound source evolution to quantitatively analyze the contribution of each mode to the far-field noise. Dynamic Mode Decomposition (DMD), as a data-driven modal decomposition technique, approximates the temporal evolution operator from time-resolved snapshots and decomposes an unsteady field into spatial-temporal modes with specific frequencies, growth/decay rates, and spatial structures. Applying DMD to these flow and sound source fields can separate coherent structures according to their characteristic frequencies and growth rates, thereby establishing a more direct link between vortex structures development and its contribution to flow-induced noise.

CRediT authorship contribution statement

Chao Chen: Formal analysis, Methodology, Software, Validation, Visualization, Writing – original draft, Writing – review & editing. **Jie Zhu:** Funding acquisition, Resources, Validation, Writing – original draft. **Liushuai Cao:** Funding acquisition, Project administration, Resources, Supervision, Validation, Writing – original draft, Writing – review & editing. **Decheng Wan:** Funding acquisition, Project administration, Resources, Writing – original draft, Writing – review & editing.

Declaration of competing interest

The authors declare that they have no known competing financial interests or personal relationships that could have appeared to influence the work reported in this paper.

Acknowledgments

This work is supported by the National Natural Science Foundation of China (Nos. 52571360 and 52131102), to which the authors are most grateful.

Appendix A. Table of Symbols and Abbreviations

Since this paper involves a large number of physical quantities and abbreviations, we added a table of symbols and abbreviations to uniformly define the units and physical meanings of each symbol to improve readability.

Table A.1
Table of symbols and abbreviations

symbol	physical meaning	unit
x_i, x_j	coordinate components	m
$\overrightarrow{u}$	fluid velocity vector	$m \cdot s^{-1}$
u_i, u_j	components of $\overrightarrow{u}$	$m \cdot s^{-1}$
u_i', u_j'	fluctuating velocity components	$m \cdot s^{-1}$
ρ	fluid density	$kg \cdot m^{-3}$
p	pressure	Pa
S_j	generalized source term	
k	turbulence kinetic energy	$J \cdot kg^{-1}$
σ_k	constant	
P_k	production term	
μ_t	turbulence viscosity	Pa·s
μ	dynamic viscosity	Pa·s
σ_k	constant	
ω	dissipation rate	
F_l, α, σ_ω, $\sigma_{\omega 2}$	constants	
$\widetilde{f}_d$	empirical function	
f_e	lifting function	
l_{RANS}	turbulence length scale of RANS	m
l_{LES}	turbulence length scale of LES	m
p'	sound pressure	Pa
p_T'	monopole term sound pressure	Pa
p_L'	dipole term sound pressure	Pa
p_Q'	quadrupole term sound pressure	Pa
v_i, v_j	velocity component of moving surface	$m \cdot s^{-1}$
$\overrightarrow{n}$	unit normal vector on surface	
n_i	component of $\overrightarrow{n}$	
ρ_0	far-field fluid density	$kg \cdot m^{-3}$
P_{ij}	compressive stress tensors	Pa

(*continued on next page*)

Table A.1 (*continued*)

symbol	physical meaning	unit
$H(f)$	Heaviside function	
σ_{ij}	viscous stress tensor	Pa
δ_{ij}	Kronecker symbol	
T_{ij}	Lighthill stress tensor	Pa
c_0	speed of sound in the fluid	$m{\cdot}s^{-1}$
v_n	normal velocity component of moving surface	$m{\cdot}s^{-1}$
u_n	normal velocity component of fluid	$m{\cdot}s^{-1}$
M_r	the Mach number in radiation direction	
$\widehat{r}$	unit vector from a point on moving surface to observer	
$\overrightarrow{M}$	Mach number vector	
M_i	component of $\overrightarrow{M}$	
θ	local angle between $\overrightarrow{n}$ and $\widehat{r}$	°
$\widehat{r}_i$	component of $\widehat{r}$	
D_R	rotor diameter	m
n	rotational speed of rotor	rps
V_a	advance speed	$m{\cdot}s^{-1}$
J	advance ratio	
K_{Tr}	rotor thrust coefficient	
ΔK_{Tr}	K_{Tr} minus its mean value	
K_{Ts}	stator thrust coefficient	
ΔK_{Ts}	K_{Ts} minus its mean value	
K_{Td}	duct thrust coefficient	
ΔK_{Td}	K_{Td} minus its mean value	
K_T	total thrust coefficient	
ΔK_T	K_T minus its mean value	
K_Q	rotor torque coefficient	
ΔK_Q	K_Q minus its mean value	
η	overall efficiency	
$\Delta\eta$	η minus its mean value	

Appendix B. Calculation of dp/dt in Section 2.3

Following the studies of Gong et al. (2026) and Sezen et al. (2021), in the basic transport equation, the material derivative of pressure is expressed as Equation (1). Therefore, the time derivative of pressure can be obtained as shown in Equation (2).

$$\frac{Dp}{Dt}=\frac{\partial p}{\partial t}+\overrightarrow{v}\cdot\nabla p \tag{B.1}$$

$$\frac{\partial p}{\partial t}=\frac{Dp}{Dt}-\overrightarrow{v}\cdot\nabla p \tag{B.2}$$

where p, $\overrightarrow{v}$ denote the pressure and velocity in the flow field, respectively. Specifically, they correspond to the pressure and velocity values of computational cells.

In the numerical implementation, a second-order backward difference scheme is adopted, the pressure derivative and velocity at each computational cell could be expressed as Equations (3) and (4), respectively.

$$\frac{Dp}{Dt}=\frac{3p_0-4p_1+p_2}{\partial t} \tag{B.3}$$

$$\overrightarrow{v}=\frac{3X_0-4X_1+X_2}{2\Delta t} \tag{B.4}$$

where p_0 denotes the current time-step pressure, p_1 denotes the first previous time-step pressure, and p_2 denotes the second previous time-step pressure. X_0 denotes the current time-step position, X_1 denotes the first previous time-step position, and X_2 denotes the second previous time-step position. Δt is the time-step.

Finally, for the pressure-time derivative, the solution is as equation (5):

$$\frac{dp}{dt}=\frac{3p_0-4p_1+p_2}{\partial t}-\frac{3X_0-4X_1+X_2}{2\Delta t}\cdot\nabla p \tag{B.5}$$

References

Brentner, K.S., Farassat, F., 1998. Analytical comparison of the acoustic analogy and Kirchhoff formulation for moving surfaces. AIAA J. 36 (8), 1379–1386.
Celik, Ghia, U., Roache, P.J., et al., 2008. Procedure for estimation and reporting of uncertainty due to discretization in CFD applications. Journal of fluids Engineering-Transactions of the ASME 130 (7).
Cianferra, M., Ianniello, S., Armenio, V., 2019. Assessment of methodologies for the solution of the Ffowcs Williams and Hawkings equation using LES of incompressible single-phase flow around a finite-size square cylinder. J. Sound Vib. 453, 1–24.
Cokmick B W, Mc, Eisenhuth, J., 1963. Design and performance of propulsors and pump-jets for under water propulsion. AIAA J. 1 (10), 2478, 2354.
Di Mascio, A., Muscari, R., Dubbioso, G., 2014. On the wake dynamics of a propeller operating in drift. J. Fluid Mech. 754, 263–307.

Farassat, F., 2007. Derivation of Formulations 1 and 1A of Farassat. Langley Research Center, Hampton, Virginia, USA. Technical Report NASA/TM-2007-214853, NASA.
Farassat, F., Succi, G.P., 1980. A review of propeller discrete frequency noise prediction technology with emphasis on two current methods for time domain calculations. J. Sound Vib. 71 (3), 399–419.
Gong, J., Wu, Z., 2026. Numerical study on the correlation between underwater radiated noise and wake evolution of a rim-driven thruster. J. Mar. Sci. Appl. 25 (1), 15–31.
Hadipour, A., Abadi, K.A.V., Khanzadi, H., et al., 2021. Hydrodynamic analysis of noise propagation by the high skew marine propeller working in non-uniform inflow. Int. J. Appl. Mech. Eng. 26 (1), 104–121.
Hu, Y.S., Wan, Z.H., Ye, C.C., et al., 2022. Noise reduction mechanisms for insert-type serrations of the NACA-0012 airfoil. J. Fluid Mech. 941, A57.
Huang, Q., Qin, D., Pan, G., 2022. Numerical simulation of the wake dynamics of the pumpjet propulsor in oblique inflow. Phys. Fluids 34 (6).
Huang, X., Shi, S., Su, Z., et al., 2022. Reducing underwater radiated noise of a suboff model propelled by a pump-jet without tip clearance: numerical simulation. Ocean. Eng. 243, 110277.
Kojima, Y., Skene, C.S., Yeh, C.A., et al., 2023. On the origin of quadrupole sound from a two-dimensional aerofoil trailing edge. J. Fluid Mech. 958 (A), 3.
Li, F., Huang, Q., Li, J., et al., 2025. Unsteady flow structures and noise characterization under stator skew in pump-jet propulsors. Phys. Fluids 37 (8).
Li, H., Li, X., He, X., et al., 2025. A study on the flow and noise of a pump-jet propulsors in the fully appended SUBOFF hull wake. Ocean. Eng. 326, 120890.
Menter, F.R., 1994. Two-equation eddy-viscosity turbulence models for engineering applications. AIAA J. 32, 1598–1605.
Porcacchia, F., Dubbioso, G., Muscari, R., et al., 2025. Effects of flow incidence on propeller underwater radiated noise. Phys. Fluids 37 (1).
Qin, D., Pan, G., Lee, S., et al., 2019. Underwater radiated noise reduction technology using sawtooth duct for pump-jet propulsor. Ocean. Eng. 188, 106228.
Sezen, S., Cosgun, T., Yurtseven, A., et al., 2021. Numerical investigation of marine propeller underwater radiated noise using acoustic analogy part 1: the influence of grid resolution. Ocean. Eng. 220, 108448.
Shi, S., Tang, W., Huang, X., et al., 2022. Experimental and numerical investigations on the flow-induced vibration and acoustic radiation of a pump-jet propulsor model in a water tunnel. Ocean. Eng. 258, 111736.
Shur, M.L., Spalart, P.R., Strelets, M.Kh, et al., 2008. A hybrid RANS-LES approach with delayed-DES and wall-modelled LES capabilities. Int. J. Heat Fluid Flow 29, 1638–1649.
Siemens, 2023. STAR-CCM+ User Guide Version 18.02. Simcenter STAR-CCM+ CFD software.
Su, J., Wang, Y., Li, F., et al., 2026. "Development of a Standard Series for Pump-Jet Propulsors and Data-Driven Regression for Performance Prediction,". Int. J. Nav. Archit. Ocean Eng., 100765
Tong, X.D., Chen, H.Y., Chen, Y., 2021. Low frequency broadband noise radiated by highly skewed propeller ingesting inflow turbulence. J. Sound Vib. 490, 115709.
Turner, J.M., Kim, J.W., 2022. Quadrupole noise generated from a low-speed aerofoil in near-and full-stall conditions. J. Fluid Mech. 936 (A), 34.
Wu, J., Yangzhou, J., Ma, Z., et al., 2023. Numerical study of rotor unsteady forces and noise due to ingestion of grid-generated turbulence. Phys. Fluids 35, 015141.
Xie, B., Han, H., Zhuang, Y., et al., 2025. Flow noise induced by an underwater vehicle with appendages. Phys. Fluids 37 (8).
Xie, B., Shen, Z., Cao, L., et al., 2026. Effects of tip vortex cavitation on the hydrodynamic and hydroacoustic performance of a marine propeller. Ocean. Eng. 359, 126007.
Yang, C., Sun, C., Wang, C., et al., 2024a. Serration of the duct trailing edge to affect the hydrodynamics and noise generation for a pump-jet propulsor. Phys. Fluids 36 (1).
Yang, C., Sun, C., Wang, C., et al., 2024b. The influence of serrated trailing edge on pulsating pressure and noise performance of pump-jet propulsor under submarine self-propulsion condition. Phys. Fluids 36 (10).
Yu, K., Park, D., Choi, J., et al., 2023. Effect of skew on the tonal noise characteristics of a full-scale sub marine propeller. Ocean. Eng. 276, 114218.
Yu, L., Wan, D., Gao, Y., et al., 2025a. The sound source distribution and mechanisms of flow-sound correlation for cavitating propellers. Ocean. Eng. 340, 122279.
Yu, L., Wan, D., Shen, Q., et al., 2025b. Numerical study of flow-sound correlation mechanism and soundsource distribution for NACA 0012 hydrofoil. Ocean. Eng. 338, 122039.
Özden, M.C., Gürkan, A.Y., Özden, Y.A., et al., 2016. Underwater radiated noise prediction for a submarine propeller in different flow conditions. Ocean. Eng. 126, 488–500.
Zhang, J., Li, H., Hua, H., 2023. Vibro-acoustic characteristics of a submarine model excited by excitation forces of pump-jet duct. J. Vib. Control 30 (11–12), 2728–2741.
Zhang, X., Liu, Z., Cao, L., et al., 2022. Tip clearance effect on the tip leakage vortex evolution and wake instability of a ducted propeller. J. Mar. Sci. Eng. 10 (8), 1007.
Zheng, S., Huang, Q., Zhou, L., et al., 2024. Effects of propeller boss cap fins on hydrodynamics and flow noise of a pump-jet propulsor. Phys. Fluids 36 (9).